Crystal growth and design Main Manuscript for

Ultrastructural features of bacterial calcite unveil ubiquitous organics occlusion and clues on biomineralization

Franco Grosso Giordano[1,2,3 *], Martín Purino[4], Nico Boon[1], Nele De Belie[2] and Carlos Rodriguez-Navarro[3*]

[1] Ghent University, Center for Microbial Ecology and Technology (CMET), Frieda Saeysstraat 1, 9052, Ghent, Belgium.

[2] Ghent University, Magnel-Vandepitte Laboratory, Dept. of Structural Engineering and Building Materials, Technologiepark Zwijnaarde 60, B-9052, Ghent, Belgium.

[3] University of Granada, Department of Mineralogy and Petrology, 18002, Granada, Spain.

[4] Ghent University, Department of Organic and Macromolecular Chemistry, Krijgslaan 281 S4, B-9000 Ghent, Belgium.

*Corresponding authors: Franco.GrossoGiordano@UGent.be; CarlosRN@Ugr.es.

Keywords: Bacteria, biomineralization, organics occlusion, amorphous calcium carbonate, calcite.

This PDF file includes:

Title page (title, author list, classification, keywords)

Abstract

Main Text

Figures 1 to 6

22 References

23

24 **Abstract**

25 Microbially-induced calcium carbonate precipitation is a widespread natural
26 phenomenon with numerous technical applications. Recent advances have shown
27 that bacterial calcium carbonates (BCC) form non-classically via amorphous calcium
28 carbonate (ACC) precursors in the presence of organics, but the role of organics in
29 the formation and nanostructural features of BCCs is not fully understood. Here we
30 show that two bacterial strains produce BCCs with diverse textural and structural
31 features at the macroscale but similar at the micro and nanoscale. We show that
32 bacterial organics guide precipitation of calcite, stabilizing ACC to produce
33 nanogranular crystals and these organics are then trapped within the crystal, rather
34 than being released as previously suggested. These organics are N-rich and create
35 regions of low Z-contrast aligned perpendicular to the *c*-axis of the crystal, yielding a
36 "Swiss cheese-like" mesostructure. Moreover, it is these occluded organics that lead
37 to the distinctive biosignatures observed in BCC. Finally, we also observe crystalline
38 2D-films, possibly proteins, templating the oriented crystallization of calcite. These
39 ultrastructural features help to disclose how microbial $CaCO_3$ biomineralization takes
40 place leading to improved technical applications and may provide fingerprints for
41 their identification in nature.

42

43 **Introduction**

44 Biomineralization is a widespread, cross-kingdom phenomenon whereby organisms
45 induce or control the formation of a variety of minerals in or around them [1]. A widely
46 occurring biomineralization process is the precipitation of calcium carbonate. It forms
47 the basis of many current biominerals structures – including shells of molluscs, the

48 cell wall of coralline algae, and the cystolith of plants [1–3] – and ancient – it is the
49 main mineral fraction in microbialites, some of the oldest fossils in the world [4]. The
50 bioprecipitation of calcium carbonate is also a common occurrence in the present day
51 microbial world [5–7], usually denominated as microbially-induced carbonate
52 precipitation (MICP). While calcium carbonate biominerals in eukaryotes is
53 considered to be tightly controlled by genetic and biochemical factors, MICP,
54 generally an extracellular phenomenon, has long been considered uncontrolled with
55 no specific purpose or functionality [8]. However, recent evidence is questioning this
56 notion [9]. For example, calcium carbonates have been reported to lead to an
57 evolutionary benefit by increasing the pathogenic capacity of strains [10], facilitating
58 biofilm formation [11], and providing survival strategies in extreme conditions [12].
59
60 Certain aspects of the biochemical understanding of MICP are well agreed upon. For
61 instance, the metabolic pathways of bacterial calcium carbonate (BCC) production
62 are in general well-known and include sulphate reduction [13], photosynthesis [2],
63 denitrification [14] ureolysis and ammonification [15] and metabolism of organic acids
64 [16,17]. They all result in alkalinization, thereby fostering the formation of CO_3^{2-} ions
65 and enabling precipitation of $CaCO_3$ in the presence of Ca^{2+} ions. Moreover,
66 researchers recognize that there is a role of extracellular polymeric substances (EPS)
67 - which include polysaccharides, proteins and nucleic acids - in the formation of
68 precipitates, acting as a Ca^{2+} adsorption template [18]. Besides their role in
69 concentrating Ca^{2+}, there is growing evidence showing that the organic-mediated
70 formation of amorphous calcium carbonate (ACC) by prokaryotes prior to
71 crystallization of anhydrous $CaCO_3$ crystals appears to be a general phenomenon [19–
72 22]. Recently, Enyedi et al. [23], showed that bacterial EPS led to long-term stabilization
73 of ACC, and suggested that the stabilized ACC eventually led to the formation of

74 calcite through non-classical crystallization. However, the MICP crystallization
75 mechanisms are still poorly understood, specifically when the role of organics is
76 involved, while structural aspects of these biocrystals have not been fully
77 characterised. This is an important research gap given MICP occurs with a wide
78 range of organisms and it has attracted a large amount of research in bio-
79 engineering applications [7].
80
81 In this work, we aim to shed light on the formation mechanism of MICP and study
82 the elemental, compositional and (ultra)structural characteristics of BCCs at multiple
83 scales. To achieve this goal we have performed crystallographic, compositional,
84 textural and (nano)structural analyses of BCCs (calcite) from two bacterial species,
85 using inorganic calcite as control. Differences between BCCs and inorganic calcite
86 were starker than between BCCs of the two species and were attributed to the
87 presence of (N-rich) organic biosignatures. Furthermore, BCCs formed through non-
88 classical ACC-to-calcite precipitation and produced mesocrystals with a Swiss-cheese
89 like structure with regions of occluded intracrystalline organic matter. In addition, a
90 bacterially-derived 2D crystalline film was identified which enabled the oriented
91 nucleation of bacterial calcite, supporting the role of organic molecules in BCC
92 formation.
93
94 **Materials and Methods**
95
96 **Synthetic calcite preparation**
97 Calcite was produced synthetically in order to act as an abiotic control. A reaction
98 pathway was chosen as proxy to that expected in the bacterial cultures, whereby
99 calcite precipitated by the dissolution of CO_2 from bacterial respiration. A saturated

100 calcium hydroxide solution was prepared by adding 5 g $Ca(OH)_2$ to 100 ml of distilled
101 water, stirring for 30 min at 50 RPM and letting sit for 2 h. The supernatant (i.e., a
102 saturated solution of Ca^{2+} and OH^- (equation 1) was poured into a clean container.
103 CO_2 was then purged through this solution. This enabled the fast dissolution and
104 hydration of CO_2, creating bicarbonate (equation 2) and carbonate ions (equation 3).
105 Subsequently, $CaCO_3$ spontaneously precipitated through the reaction of carbonate
106 ions with Ca^{2+} (equation 4) in the absence of any background electrolyte. The
107 precipitates were filtered using a vacuum pump and polycarbonate filters (φ = 0.22
108 µm). The filter with the precipitates was placed at room temperature (*T*) and dried
109 overnight. The dry solids were stored in plastic vials for further analysis.
110

111 $$Ca(OH)_2 \rightarrow Ca^{2+} + 2OH^- \quad (1)$$

112 $$OH^- + CO_2 \rightarrow HCO_3^- \quad (2)$$

113 $$HCO_3^- + OH^- \rightarrow CO_3^{2-} + H_2O \quad (3)$$

114 $$Ca^{2+} + CO_3^{2-} \rightarrow CaCO_3 \quad (4)$$

115

116 **Selection and cultivation of bacterial strains**

117 Two bacterial strains were used in this study, *Lynsinobacillus fusiformis* (LMG 9816)
118 and a recently isolated strain, *Shouchella clausii* (registered at the Belgian
119 Coordinated Collection of Microorganisms as LMG 33400). *S. clausii* was isolated
120 from a lime mortar wall in Ghent, Belgium by selecting morphologically distinct
121 colonies from a Horikoshi medium. Its capacity for carbonate precipitation was tested
122 on pH 8-adjusted B4-medium (0.4 % yeast extract, 0.5 % dextrose, 0.265 % Ca-
123 acetate hydrate, 1.4 % agar, adjust pH to 8 using 0.1M NaOH), a standard medium
124 used to study precipitation of calcium carbonate crystals [5,23–25]. Importantly, Ca-
125 acetate was filter sterilized as doing otherwise would lead to precipitation of calcium

126 carbonate either through too high pH or through heating of the Ca-acetate. Finally,
127 the strain was selectively adapted to high pH tolerance by repeated inoculation in
128 TSB adjusted to pH 11 with CAPS buffer. An alkaliphile was desirable as MICP
129 commonly occurs in alkaline environments. The bacteria were grown and kept in TSA
130 at 28 °C.
131

132 **Culture and precipitation media, and precipitate extraction**

133 Due to the alkaliphilic nature of both bacteria, carbonate precipitation experiments
134 were carried out on pH 8-adjusted B4-medium. For the inoculation of B4 plates,
135 bacteria were inoculated in TSB and grown for 48 h. Subsequently, 10 µL of a fully
136 grown culture was drop-inoculated onto 9 spots on B4 plates. The cultures were
137 grown for 4 weeks at 28 °C. At this point, precipitates were visible on the plate and
138 were extracted. Briefly, the B4 agar was cut into pieces and placed in a glass
139 container and melted in a microwave oven. 100 mL of warm deionized water were
140 added to the beaker to dilute the melted agar. The dilute agar was centrifuged at
141 5000 rpm for 1 min while still warm. The pellet was then microwaved again, warm
142 water was added, and centrifuged again. This was performed a third time but
143 centrifuged at 7000 rpm. The sample was warmed up once more, and the suspension
144 was filtered using a vacuum pump and polycarbonate filters (φ = 0.22 µm). The
145 filter with the precipitates was placed at room temperature and dried overnight.
146 Once dried, the solids were placed in a plastic vial for further analysis.
147

148 **Bleaching of precipitates**

149 A fraction of the bacterial precipitates was bleached to remove any potential organic
150 matter on their surfaces [26]. Bleaching was done using commercial bleach and
151 deionized water (1:1 dilution) poured in an Eppendorf tube (1.5 mL) filled with 0.1 g

152 solids, followed by incubation for 2 h in a shaking table. The samples were then
153 centrifuged for 1 min at 5000 RPM and the supernatant discarded. Bleached solids
154 were resuspended in MilliQ water, vortexed for 1 min, and centrifuged again.
155 Washing was performed thrice. The precipitates were dried at 50 °C overnight.
156
157 **FTIR spectroscopy**
158 Fourier Transform Infrared Spectroscopy (FTIR) spectra of the precipitate were
159 recorded on a NICOLET 20SXB FTIR (400–4000 cm^{-1} spectral range; resolution of 2
160 cm^{-1}). Baseline and smoothing corrections to the FTIR spectra was performed using
161 Spectragryph v1.2.16.1.
162
163 **X-ray diffraction (XRD)**
164 The crystallographic features of the synthetic (control) and bacterial precipitates
165 were analysed with a Xpert Pro X-ray powder diffractometer (Panalytical, The
166 Netherlands) in reflection mode using copper radiation to determine θ−2θ scans
167 (measurement parameters: Cu Kα radiation λ = 1.5405 Å, 45 kV, 40 mA, 3 to 70°
168 exploration range, with 0.00418° step size and 29.8 s integration time per step).
169 Bacterial precipitates were analysed in zero-background Si sample holders. XRD
170 patterns were analysed using the computer program HighScore Plus Version 3.0d.
171
172 **TG analysis**
173 Thermogravimetric analysis (TGA) was performed using a TGA 2 (Mettler-Toledo,
174 Switzerland) with a large furnace and an autosampler, using 70 µL alumina crucibles.
175 Samples (12 mg) were heated at 20 °C/min from 25 to 950 °C under air atmosphere
176 (80 mL/min).
177

178 **Synchrotron High-Resolution Powder X-Ray Diffraction (HRXRD)**

179 HRXRD analyses were performed at beamline CRYSTAL of the SOLEIL synchrotron
180 (Paris, France). The wavelength 0.672356 Å (18.44024 keV) was selected with a
181 double-crystal Si (111) monochromator and determined by using Si640d NIST
182 standard (a = 5.43123 Å). The CRYSTAL beamline is equipped with a high-
183 throughput position sensitive detector (PSD) MYTHEN, optimal for time-resolved
184 experiments. Borosilicate glass capillaries of 0.3 mm diameter were loaded with
185 powder samples and rotated during data collection to improve diffracting particle
186 statistics. Isochronous annealing (10°C min^{-1}; 30 s stabilization time at target T,
187 tolerance ± 5°C) was performed using a Cyberstar hot gas blower with a Eurotherm
188 T controller (Eurotherm, Worthing, UK), collecting diffraction data each 50°C during
189 the heating ramps (50° to 400°C). Once the maximum T was reached, the samples
190 were cooled to room T, and a final measurement was taken. The data acquisition
191 time was ~5 min per pattern, with up to two iterations per measurement to obtain a
192 good signal-to-noise ratio over the 0-55.34 °2θ angular range. To calibrate the
193 equipment and reduce possible shifts during experimental analysis, a LaB6 standard
194 was used. An instrumental resolution factor analysis was performed in each case.
195 Under these data acquisition conditions, the angular resolution was better than
196 0.006° FWHM. As opposed to conventional XRD, such an angular resolution enables
197 to detect lattice strains of 10^{-3} to 10^{-4} associated with intracrystalline organics.
198

199 The Rietveld refinement method [27] was used to extract lattice parameters of calcite
200 matching the experimental diffraction peaks with those included in Markgraf and
201 Reeder [28] using Topas software. Optical quality (highly pure) geologic calcite (Iceland
202 spar, from Chihuahua, Mexico) was used as standard to compare XRD data from
203 BCC.

To investigate the microstructural variations due to organic (macro)molecule incorporation in the calcite structure, the Thompson-Cox-Hastings pseudo-Voigt function was used to fit the profile of the experimental diffraction patterns. Refinement cycles were performed to ensure reproducibility of each analysis, selecting a Goodness of Fit of <9. Note that, as opposed to BCC, in the case of the Iceland spar control no changes in Bragg peak position or broadening (FWHM) were observed after annealing, i.e., after returning to room *T* following heating up to 400°C. These results show that the selected geogenic calcite is a proper reference to compare the results of BCC HRXRD analysis.

FESEM and TEM analysis

Field Emission Scanning electron microscopy (FESEM) images were collected using an Auriga (Zeiss, Germany) microscope with field emission gun operated at 5 kV. All samples were carbon coated prior to imaging.

Nanoscale features and elemental composition of the precipitates were studied using TEM on a Titan (FEI) with acceleration voltage of 300 kV. The TEM was equipped with a high angle annular dark field (HAADF) detector for Z-contrast imaging and energy dispersive X-ray spectroscopy (EDS) for microanalysis (performed in STEM mode). Right before TEM analysis the solids were dispersed in ethanol, sonicated for 2 min and fished with carbon-coated TEM Cu grids. Imaging was performed using a 20 μm objective aperture, which is a good compromise for amplitude and phase contrast (high resolution, HRTEM) imaging. Selected area electron diffraction (SAED) patterns were collected from areas ~200 nm in diameter.

230 **Solid-state NMR (ssNMR)**

231 The 1D experiments were recorded on a Bruker Ascend 500.13MHz Avance III
232 spectrometer equipped with a Bruker broadband 4 mm 1H/X dual channel CP-MAS
233 smartprobe probe head, equipped with Z-gradients, a MAS III pneumatic unit and
234 running Topspin 3.6.5. For each measurement, the spinning frequency was set to
235 12000Hz, all measurements were performed at room temperature (25°C) and
236 controlled with a Eurotherm 2000 BVT controller and a BCU-I.

237

238 All samples were prepared by filling the 4mm Bruker K1910 ZrO2 rotors with an
239 appropriate amount of dry and finely grained sample material (25-30 mg per
240 sample). Using subsequent rounds of filling and packing the rotor led to a tightly
241 filled rotor sample for each material under study. Following the packing of the rotors,
242 each of them was sealed with a Kel-F insert, a Kel-F rotor cap and visually checked
243 for any leftover voids or air pockets.

244

245 The spectra recorded on the samples included 1D ^{1}H and 1D ^{13}C measurements. For
246 the 1D ^{1}H 'onepulse' experiments, the spectral width used was 200.00 ppm with 4
247 scans of 4K data points each being accumulated, preceded by 2 dummy scans and a
248 relaxation delay of 2 seconds. Finally, the spectrometer excitation frequency was set
249 on resonance with the frequency (5 ppm) of the most intense signal. Processing
250 consisted of one order of zero filling to 16K real data points, followed by Fourier
251 transformation, phase correction and a base-line correction.

252

253 For ^{13}C measurements a 'hpdec' measurement type was used for non-cross-
254 polarization and 'hX.cp' for measurements with cross-polarization (CP) with ^{1}H. The
255 spectral width used was 300.00 ppm with 2048 scans of 4K data points each being

accumulated, preceded by 4 dummy scans and a relaxation delay of 5 seconds. Finally, the spectrometer excitation frequency was set on resonance with the frequency (100 ppm) of the most intense signal. Processing consisted of one order of zero filling to 16K real data points, followed by Fourier transformation, phase correction and a base-line correction.

Chemical shifts were indirectly referenced by adapting the magnet 'field' value -by measuring an adamantane reference sample-, and adapting the magnet field until one of the adamantane signals is at the right chemical shift value (37.77 ppm). All spectra were processed using TOPSPIN 4.1.3.

Results

BCCs have distinctive biosignatures associated with organics and ACC

The calcium carbonate precipitating capacity of two bacterial species was studied. *Lynsinobacillus fusiformis* (LMG 9816) strain was selected as it has been commonly used in other studies of MICP [29,30]. To test whether nanoscale characteristics between BCCs were similar, a recently isolated strain producing morphologically distinct BCC, *Shouchella clausii* (previously known as *Alkalohalobacillus clausii*) LMG 33400, was used. No previous *Shouchella* (or *Alkalohalobacillus)* strain has been reported to precipitate calcium carbonate.

Optical microscopy imaging (Figure 1a,e) disclosed morphological differences between mineral precipitates produced by *L. fusiformis* and *S. clausii*. *L. fusiformis* mainly produced irregular precipitates with spherical incrustations, while *S. clausii* induced the formation of spherical or oval-shape precipitates. A detailed observation

282 of the latter shows that they display elongated disphenoidal forms, or spindle- and/or
283 dumbbell-shaped structures, as also observed in other bacterial species [31]. Such
284 diverse precipitate morphologies have been observed for different bacteria in studies
285 using the same standard culture medium used here (B4) [24]. Both bacteria produced
286 precipitates associated with the bacterial colonies as well as in the surrounding
287 media. Field emission scanning electron microscopy (FESEM) analysis showed the
288 presence of carbonate precipitates closely-associated with organic matter (Figure 1b,
289 f). At the microscale all precipitates had an overall rhombohedral morphology,
290 consistent with the presence of calcite (see XRD results below) and were better
291 developed in the case of *S. clausii* samples (Figure 1d vs g and h). All of them
292 showed a nanogranular texture, implying formation through particle attachment
293 (PA). In PA, ACC particles 100 – 400 nm in size [32] in the presence of organics [33] or
294 crystalline $CaCO_3$ nanoparticles [34], attach forming a single crystallographic unit and
295 this is typically observed in carbonate biominerals produced by a range of organisms
296 (e.g., molluscs, barnacles, echinoderms, cnidaria) [26,35–37], including other bacteria [23].
297 The precipitates were bleached to remove any organics on the precipitate surface
298 and study possible crystallographic and compositional changes. After bleaching,
299 organic matter was not observable anymore on the precipitates (Figure 1c, d and h),
300 calcified bacterial casts could be spotted (Figure 1c), and the crystallographic faces
301 were more obvious (Figure 1h). Note that we performed bleaching tests with
302 increasing reaction time from 10 up to 480 min, observing (using FTIR) that the
303 removable fraction of organics could not be detected after 10 min (see Supporting
304 Information and Supporting Figure 1 and Supporting Figure 2).
305

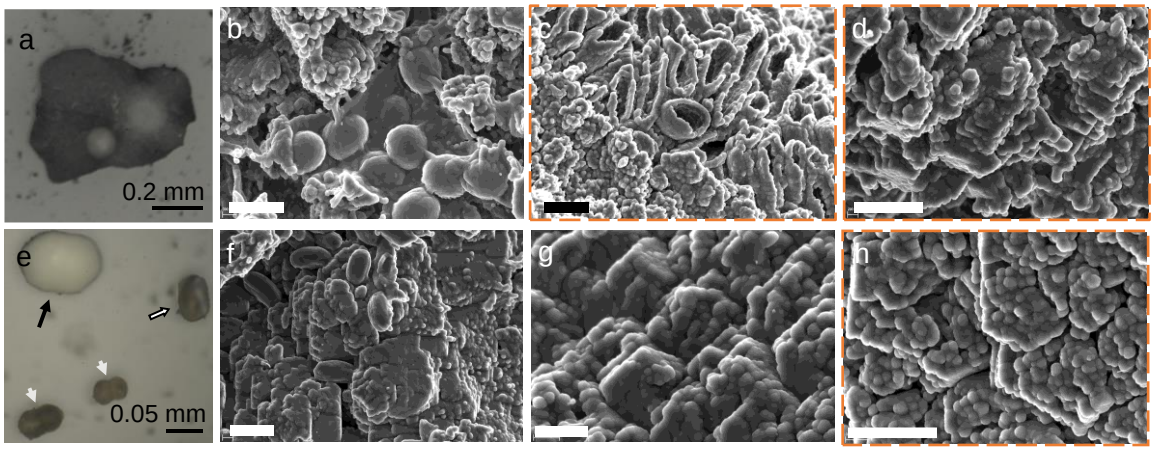

Figure 1. Optical and scanning electron microscopy photomicrographs of bacterial calcium carbonate. Calcium carbonate structures precipitated by *L. fusiformis* (a - d) and *S. clausii* (e - h). Orange outlined images are samples treated with bleach (c, d, h). Different morphologies of calcium carbonate precipitates were produced by both bacteria. (**a**) *L. fusiformis* produced irregular precipitates. (**b**) Bacteria and biofilm associated with precipitated calcium carbonate. (**c**) Bleached *L. fusiformis* precipitates showing the calcified bacterial casts. (**d**) Bleached *L. fusiformis* precipitates (showing rhombohedral vicinal faces) made up of ordered nanoparticles. (**e**) *S. clausii* produced ovoidal (black arrow), disphenoidal (white arrow with black outline) and dumbbell (white arrows) shaped precipitates. (**f**) *S. clausii* cells associated with precipitated calcium carbonate (calcite rhombohedra). (**g**) Detail of the mesostructured $CaCO_3$ crystals. (**h**) Bleached calcium carbonate showing the orderly arrangement of calcium carbonate nanoparticles. In all cases the shapeless precipitate subunits varying between 100 – 200 nm in size are distinguishable within calcite mesocrystals. All SEM micrograph scale bars are 1.2 µm.

XRD confirmed the precipitation of calcite rather than any other calcium carbonate polymorphs. The humps at 10 and 20 - 30 °2θ in the XRD patterns of both *S. clausii*

326 and *L. fusiformis* carbonates pointed to the presence of two distinct amorphous
327 phases (Figure 2a). Note that no humps were present in the XRD pattern of abiotic
328 calcite (control). Changes in the relative intensity of Bragg peaks were observed for
329 BCCs, as compared with synthetic calcite. Notably, the intensity of the 110 Bragg
330 reflection increased drastically (as compared to the main 104 Bragg reflection). The
331 (11.0) plane is associated with crystals elongated along the *c*-axis [38] and consistent
332 with the crystal morphology observed in Figure 1. Overdevelopment of {11.0} faces,
333 or more exactly, pseudo-faces composed of (01.2) and (11.0) forms [39], is common in
334 - although not exclusive to - other calcite biominerals and abiotic calcite formed via
335 ACC-to-calcite crystallization in the presence of organics (see Supporting
336 Information). After bleaching, both humps at 10 °2θ and 20-30 °2θ disappeared.
337 The bleaching of precipitates also led to changes in the intensity of Braggs peaks of
338 both bacterial crystals, most starkly non-(104) planes, with 110 and 113 Bragg
339 reflections being the strongest (Supporting Table 1). We observed better
340 development of crystal faces after bleaching (Figure 1c, d and h) which would explain
341 the XRD changes.
342

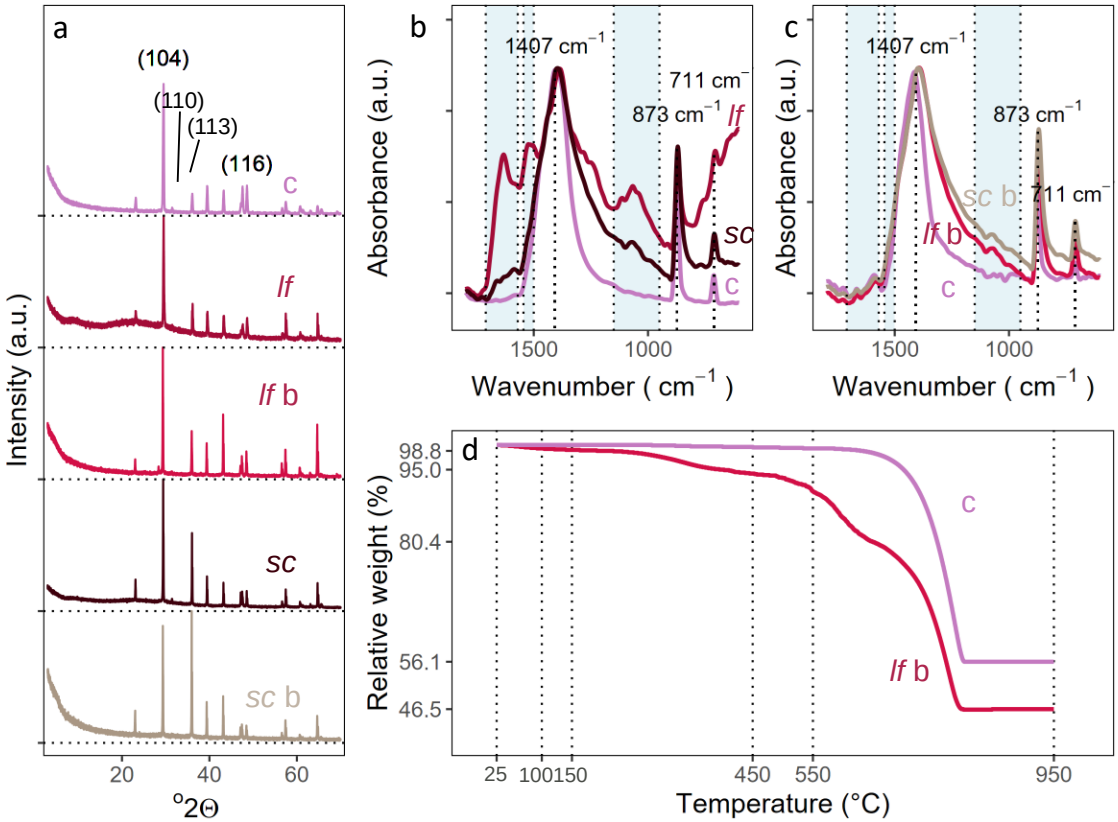

Figure 2. Analysis of synthetic (c, purple) and bacterial crystals (*L. fusiformis* (*lf*, red) and *S. clausii* (*sc,* brown)). Both bacterial calcites were bleached to remove organic matter from the surface (*L. fusiformis* (*lf* b, light red) and *S. clausii* (*sc* b, light brown)) **(a)** XRD patterns of the studied calcium carbonates. Bragg peaks correspond to calcite in all cases and the main *hkl* reflections are indicated. **(b)** FTIR spectra of synthetic, *L. fusifomis* and *S. clausii* calcites. Blue shaded bands indicate organic and/or ACC wavenumber regions. **(c)** FTIR spectra of the calcites after bleaching **(d)** TGA of *L. fusifomis* bleached calcite (light red) vs synthetic calcite (purple).

FTIR spectroscopy showed distinctive spectral features among the different precipitates. All precipitates displayed the characteristic v_2, v_3 and v_4 bands of calcite

356 at 873, 1407 and 711 cm^{-1}, respectively, however with some differences. Bacterial
357 calcites showed a slightly red-shifted v_2 band at 869 cm^{-1} (with a broad tail spanning
358 to lower wavenumbers) and a v_3 band at 1402 cm^{-1}. The red-shift of the v_2 band can
359 be caused by ACC which has a characteristic band at 860 cm^{-1} also seen in ACC
360 producing bacterial strains [3,40–43]. There were also variations in the absorbance of the
361 v_2 and v_4 bands. Synthetic calcite had the sharpest and strongest absolute v_4
362 absorbance followed by *S. clausii* and finally by *L. fusiformis* (Figure 2b). Besides the
363 differences in the vibrational modes, certain bands were evident in biogenic
364 precipitates but absent in synthetic calcite: namely between 950 – 1150 cm^{-1}, at
365 1500 – 1550 cm^{-1}, and between 1570 – 1700 cm^{-1}. A last band became apparent at
366 1190 - 1350 cm^{-1}, characteristic of amides [23], when subtracting the synthetic calcite
367 with the BCC spectra (Supporting Figure 3). Similar spectra have been previously
368 reported on bacterial calcites [23,43,44], attributed to overlapping signatures of organics
369 (general organics at 950 – 1150 cm^{-1} and amides at > 1500 cm^{-1}) and ACC (v_1-mode
370 1060-1080 cm^{-1}; a v_3 asymmetric vibration at 1470 cm^{-1}; and O-H bending at 1650
371 cm^{-1} from structural H_2O in ACC) (for details see Supporting Information). As such,
372 Mehta and colleagues [43] concluded that it is difficult to infer the presence of ACC
373 from the bands at > 900 cm^{-1} alone.
374
375 Following the bleaching process used to remove organic matter, BCCs produced
376 almost matching FTIR spectra (Figure 2c). No shift was observed in the carbonate v-
377 modes, yet all three modes experienced an increase in absorbance. This is important
378 as changes in calcite v-mode absorbance, most notably the increase in intensity of
379 the 712 cm^{-1} band, is associated with an increase in crystallinity of the carbonates [41].
380 However, the lack of shift in the v_2 band, and in particular the persistence of the
381 right broad tail, suggests that some ACC was still present, most likely structurally

382 bound to the BCC calcite structure. Conversely, the increase in v_4 absorption after
383 bleaching suggests that a fraction of ACC, likely the superficially exposed (see TEM
384 results below), was transformed into calcite via dissolution-precipitation in the bleach
385 solution, and/or was removed after rinsing of the bleach. Moreover, the bleaching
386 process leads to removal of bands at higher wavenumbers (bands at 1500 – 1550
387 cm^{-1} and 1570 – 1700 cm^{-1}), previously linked to organics. On the contrary, the
388 bands at 950 – 1150 cm^{-1} and 1190 – 1350 cm^{-1} also corresponding to organics and
389 ACC were conserved after bleaching, with a reduction in absorbance, especially in *L.*
390 *fusiformis*. Interestingly, the amide-specific band at 1190 – 1350 cm^{-1} in *L.*
391 *fusiformis* BCC experienced a shift to higher wavenumber after bleaching. Given that
392 we can associate the wavenumber to the bond strength, a higher wavenumber
393 means that a stronger bond exists between the remaining organics and the crystal
394 structure [45]. It follows that bleaching removed the material more weakly associated
395 with the BCC crystals (e.g. adsorbed organics and ACC), and the subsequent rinsing
396 of the bleach led to dissolution of precursor ACC and recrystallization of calcium
397 carbonate on certain preferential faces of the crystals. This would be responsible for
398 the disappearance of the two humps in the XRD patterns and the changes in Bragg
399 peak intensities. Nevertheless, a fraction of organics (and likely ACC) were not
400 affected by the bleaching process, as a signal of organics remains in the FTIR
401 spectra. Duplicates of the BCCs before and after bleaching show consistent FTIR
402 bands (see Supporting Information and Supporting Figure 4).
403
404 Thermogravimetric analysis (TGA) was performed on the bleached BCCs of *L.*
405 *fusiformis* and synthetic calcite to further disclose the compositional nature of the
406 biominerals (Figure 2e). The calcite control shows a weight loss of 42.3 % starting
407 from 650 °C, close to the theoretical 44 % due to the decarbonation of calcite. The

408 bleached BCC of *L. fusiformis*, showed a continuous and step-wise mass loss at $T <$
409 100 °C, 150 – 500 °C, 500 – 600 °C and 600 – 950 °C. The initial mass loss is from
410 adsorbed water. The second loss can be from ACC dehydration and/or thermal
411 decomposition of the remaining organic matter. The dehydration of ACC occurs at
412 100 – 350 °C [42,46] and the decomposition of organic matter starts at 250 °C and
413 continues up to 400 or 600 °C for intracrystalline matter [42,47]. Although there is an
414 overlap between both decompositions, the continuous mass loss after 350 °C
415 distinguishes the presence of organics. Finally, unlike the control, the weight loss of
416 BCC from 650 - 950 °C (33.9 %) does not match the value corresponding to the
417 theoretical mass loss of $CaCO_3$ following release of CO_2, but rather the weight loss
418 from 550 – 950 does (44.1 %). A lower decomposition temperature in $CaCO_3$ is
419 associated with lower crystallinity [48], which corresponds to the lower crystallinity of
420 BCCs observed with FTIR.
421
422 Overall, it becomes apparent that BCCs produced by the two bacteria studied, when
423 formed, are associated with bacterially-derived organic matter and ACC, with
424 distinctive biosignatures in all tests. FTIR confirmed that bleaching removes a non-
425 calcite fraction, seemingly composed of organics and ACC loosely bound to the
426 crystal surfaces, as seen on the SEM micrographs. But FTIR and TGA results show
427 that there is a non-removable organic/ACC fraction that is more permanently
428 associated with the BCC crystals. Overall this produces biomineralized calcite with
429 non-perfect crystal lattice (i.e. lower crystallinity).
430
431 **Organics lead to the formation of a distinctive nanostructural Swiss-cheese**
432 **like structure**

433 To further disclose how the organics were associated with the precipitates, TEM and
434 HRTEM analyses were performed, complemented with HAADF-EDS. Under the TEM
435 we observed that unbleached *L. fusiformis* precipitated crystalline (calcite) and
436 amorphous (ACC) phases as confirmed by selected area electron diffraction (SAED)
437 patterns (Figure 3a, Supporting Figure 5a). Conversely, we could not find individual
438 or aggregated ACC particles in the case of *S. clausii* which only showed single crystal
439 SAED patterns of calcite (Figure 3c). Additionally, SAED patterns with calcite single
440 crystal features were frequently arced, with spots displaying an angular spread of ~4
441 to 12° on both BCCs (Figure 3c, Supporting Figure 5a). Angular spreading is a
442 distinctive feature of mesocrystals reflecting a slight misorientation among the
443 different nanocrystals making up a mesocrystal [49] and commonly associated with the
444 presence of organic matter in biominerals [50]. The elemental composition of the
445 unbleached precipitates was confirmed with EDS mapping. Ca, O and C were
446 ubiquitous in all samples. Moreover, it was possible to correlate the presence of
447 organic-related elements such as, N, S and P – the latter two in trace amounts – in
448 the crystals produced by both bacteria (Figure 3b, d, Supporting Figure 5b,
449 Supporting Figure 6).
450

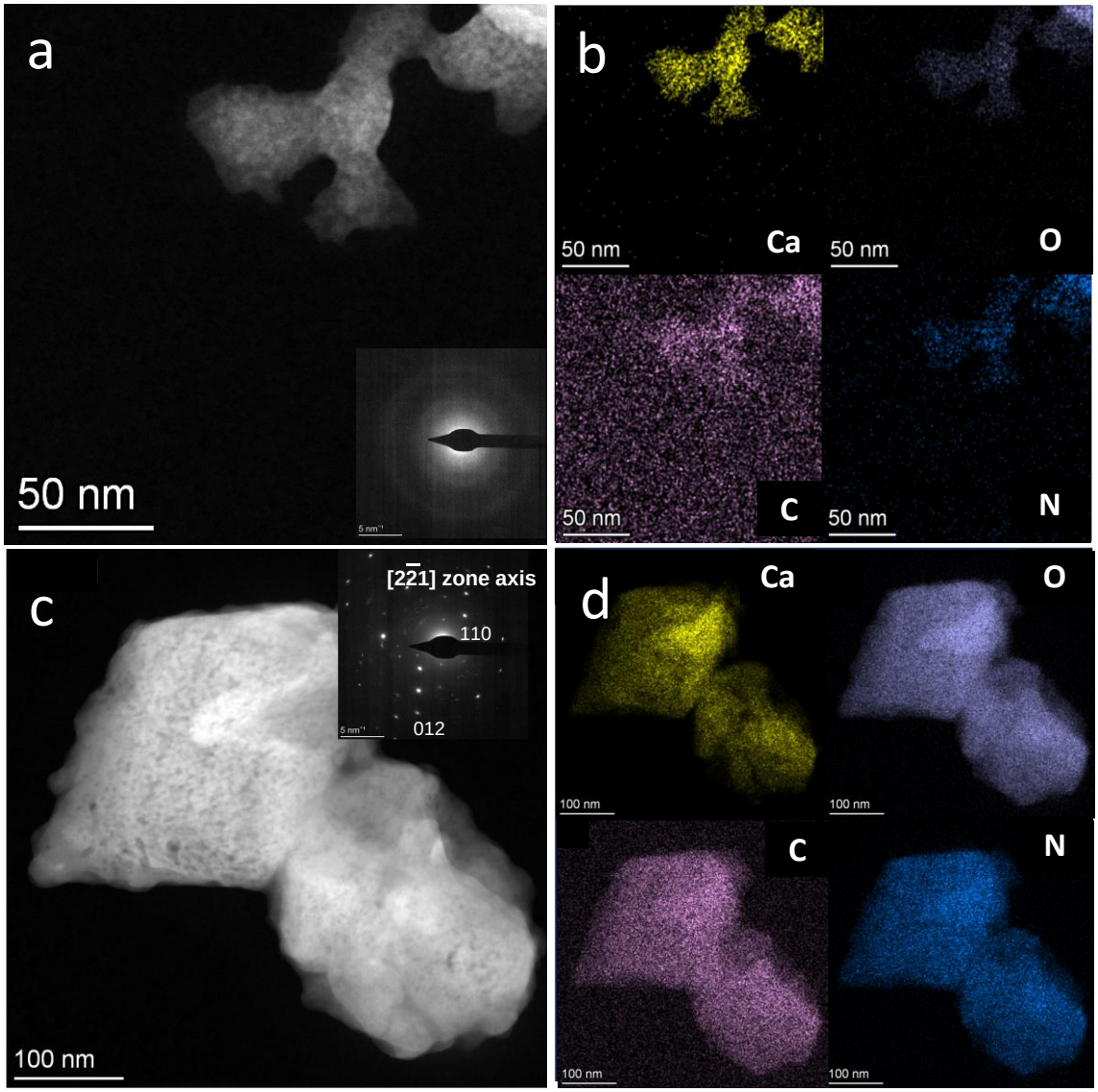

Figure 3. TEM and EDS analysis of bacterial calcium carbonates. (**a**) HAADF image of ACC precipitated by *L. fusiformis*. Inset: SAED pattern showing the amorphous nature of the particle. (**b**) In clockwise order: EDS elemental maps of precipitates in (a) (calcium, oxygen, nitrogen and carbon, respectively). (**c**) HAADF image of calcite crystals precipitated by S. clausii. Note the nanoporous structure of the crystals. Inset: [2$\bar{2}$1] zone axis SAED pattern of the calcite particle on the left with diffraction spots showing an angular spreading of 6°; (**d**) In clockwise order: EDS elemental maps of precipitates in (d) (calcium, oxygen, nitrogen and carbon,

460 respectively).

461

462 EDS line-scans from the edge to the interior of the unbleached BCC crystals showed
463 that N was not only present within the crystals but also adsorbed on their surface as
464 the intensity did not drop to zero outside the crystal (Figure **4**a-d). Point scans
465 showed a lower N:Ca ratio in the centre of the crystals than in the rim (Figure **4**e).
466 This implies that the internal areas of the precipitate include a lower relative amount
467 of organics than the rim. HRTEM was used to observe the precipitate rim more in
468 detail. In the case of *S. clausii*, lattice fringe images and corresponding FFT showed
469 that, generally, the outermost layer of the bacterial calcite crystals was amorphous,
470 confirming previous observations [23] (Figure **4**f-h, more examples in Supporting
471 Figure 7). Moreover, here we also observed amorphous areas, interwoven within the
472 crystalline lattice (Figure **4**f). This occurred in a region of intermediate contrast and a
473 few nanometers in thickness at the edge of the crystal, which was N-enriched
474 according to EDS analysis (N:Ca ratio of 0.53 Figure **4**e). The latter points to
475 occlusion of organics and/or amorphous calcium carbonate, consistent with the
476 relatively high Ca content (Figure **4**e).

477

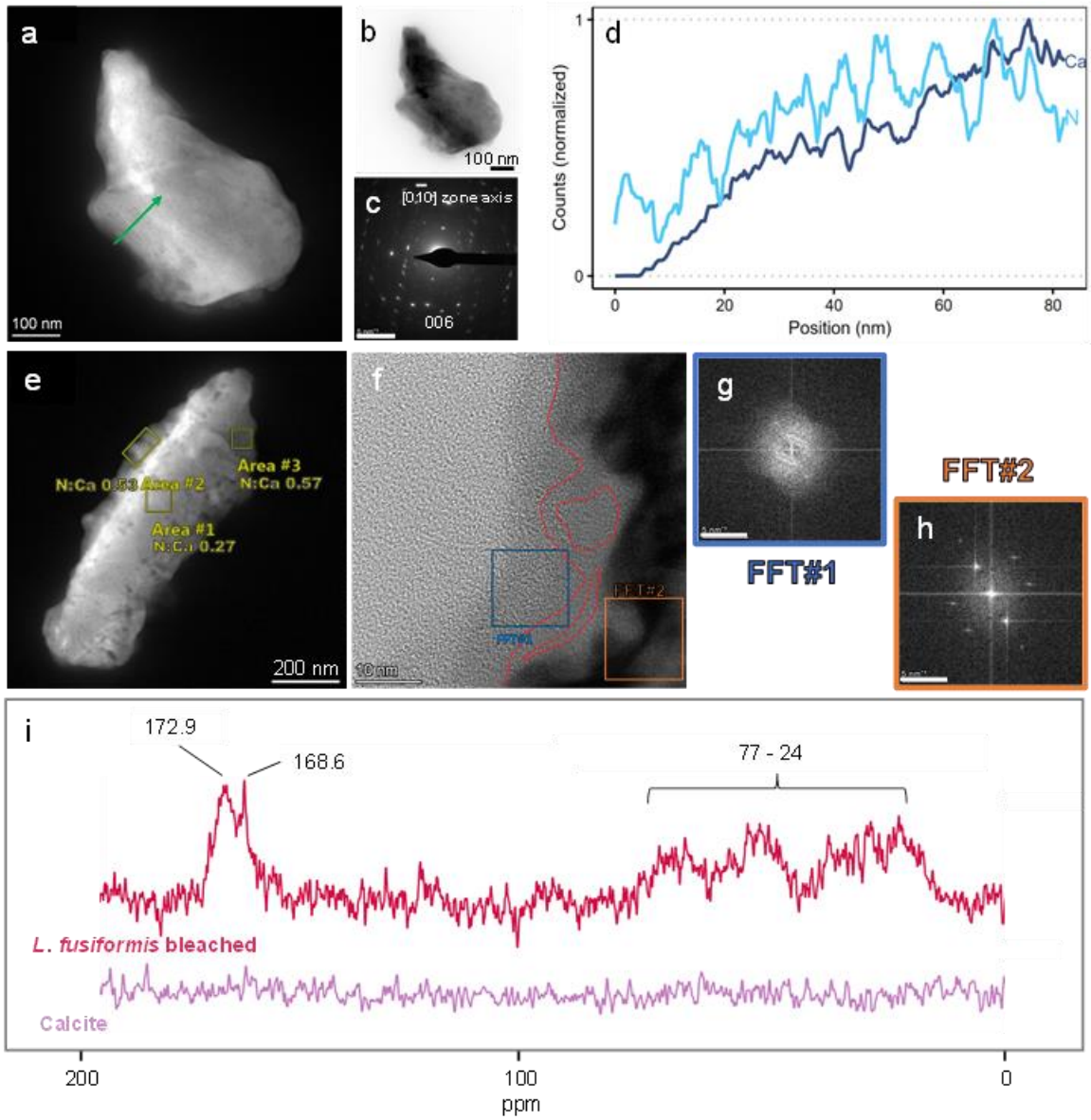

Figure 4. HRTEM, HADDF-EDS and ss-NMR analysis of bacterial calcium carbonates. (a) HAADF image of calcite crystal precipitated by *L. fusiformis*. The porous -Swiss-cheese like- structure of the calcite crystal is visible and the location of the EDS line scan is indicated (green arrow). **(b)** Brightfield TEM imagae of the crystal in (a). **(c)** [0$\bar{1}$0] zone axis SAED pattern of the crystal shown in (a) and (b). Note the marked arcing of diffraction spots (showing an angular spreading of ~9°).

486 **(d)** Line scan in (a) showing that N concentration (light blue line) is uncoupled (after
487 40 nm) to that of Ca (dark blue line), and the increase in N can be traced to the
488 pores on the calcite crystal (corresponding to the darker areas in (a)). **(e)** *S. clausii*
489 calcium carbonate structure showing different N/Ca ratios in different areas. **(f)**
490 HRTEM image of the edge of the precipitate in (e) (Area #2) with FFT of the blue
491 squared area **(g)** demonstrating it is an amorphous external layer, and the FFT of
492 the orange squared area **(h)** showing it is a crystallized (calcite) internal zone. The
493 red outline demarcates the end of the lattice fringes, showing amorphous areas
494 trapped within the crystalline zone at the rim of the precipitate. **(i)** CP–MAS ^{13}C NMR
495 spectra of bleached *L. fusiformis* calcite (light red) and synthetic calcite (purple).
496 The peak at 172 ppm is associated with calcite while the remaining peaks are due to
497 the presence of amides. Referenced to the signal of DSS (δ = 0 ppm).

498 Furthermore, an uncoupling of N and Ca was observed on the line-scans in the inner
499 region of the crystals (> 40 nm from the edge), i.e. when Ca increased, N decreased
500 (Figure ***4***d), albeit with a slight phase-shift. Upon close inspection of HAADF images,
501 it was clear that the crystals did not show a homogenous surface (Figure ***4***a).
502 Rather, a Swiss cheese-like structure could be observed, with elongated generally
503 parallel low Z-contrast pore-like areas present within the bacterial calcite single
504 crystals (more examples in Supporting Figure 8). A direct association of these low Z-
505 contrast nanoporous-looking areas with an increase in N content was systematically
506 observed. It could be argued that this porous structure is the result of beam
507 damage. However, this is ruled out here because the HAADF images were collected
508 before EDS analysis and the porous structure was already present. Pioneering work
509 by Towe and Thompson [51], and many other subsequent studies [52] have also shown
510 that beam damage does not produce such features, but organics do. Moreover, this
511 structure was also observed in many other BCCs during brightfield TEM analysis and

512 subsequent SAED analysis showed no CaO diffraction spots/rings which are standard
513 features of beam damage in calcite [53]. Note also that we have not observed such
514 Swiss-cheese structure in any studied synthetic calcite crystal. Although a Swiss-
515 cheese-like structure has never been reported in the case of BCC, similar features
516 have been observed in other calcium carbonate biominerals, such as mollusc shells
517 [52,54], and their biomimetic counterparts [55]. The pore-like areas have been usually
518 identified as intracrystalline organic matter and recently with ACC (see Supporting
519 Information).
520
521 CP-MAS ^{13}C NMR (ss-NMR) and HRXRD were used to confirm the nature of those
522 observed here, utilizing bleached precipitates. The CP-MAS ^{13}C NMR spectra of
523 bleached BCC primarily consist of broad peaks, with a notable exception at 168 ppm
524 attributed to calcite (Figure ***4***i), as confirmed by the MAS ^{13}C of synthetic calcite
525 (Supporting Figure 9). The broad peaks are indicative of amorphous content yet no
526 well-defined peak was observed closely associated downwards of calcite (167 ppm),
527 where ACC is typically present [56]. The remaining option for amorphous content must
528 then be organic in nature. Many broad peaks are present in the 20 - 80 ppm range
529 and a peak at 172 ppm suggests the presence of carbonyl groups. These shifts are
530 linked to amino acids which have peaks at 20-60 ppm (CH), and 170-180 ppm
531 (carbonyl) [57]. Overall, the spectra closely resembles that of eggshells [58] and protein-
532 including calcite biominerals [59]. The CP-MAS ^{13}C of the synthetic calcite does not
533 show any bands, as expected (Figure ***4***i; see also Supporting Figure 9). This means
534 that the calcite peak present in the *L. fusiformis* BCC is associated with hydrogen
535 atoms, only available from either organics or water [56.] Because the presence of
536 water, such as in monohydrocalcite [56,] should broaden and shift to higher ppm values
537 the calcite carbonyl bond, we conclude that the hydrogen is from amine or carboxyl

538 groups from the organics. Lastly, the broadness of the peaks further suggests that
539 the structure is internal [56]. This suggests that the observed Swiss cheese-like
540 structure must be present through the whole crystal and not superficially as
541 seemingly observed on TEM.
542
543 To further disclose whether these regions are internal, and related to the organic
544 signatures ubiquitously observed, we performed HRXRD analyses at the CRYSTAL
545 beamline of the Soleil synchrotron (Paris, France). HRXRD analysis showed that the
546 104 and 006 Bragg peaks of bleached BCC produced by *L. fusiformis* were left-
547 shifted (i.e., to higher *d*-spacings) as compared with geogenic calcite (optical quality
548 Iceland spar) (Figure 5a, b). The shifting was more marked for the 00*l* reflections,
549 implying anisotropic lattice distortion. Rietveld full profile fitting analysis [27] yielded
550 the following refined cell parameters for BCC calcite: a = 4.98900(4) Å; c =
551 17.08345(5) Å; cell volume = 368.24(4) Å^3, demonstrating a clear anisotropic lattice
552 distortion as compared with reference geogenic calcite (a = 4.98970(2) Å; c =
553 17.05900(4) Å; cell volume = 367.82(2) Å^3). Maximum lattice strain was observed
554 along the [001] direction ($\Delta c/c$=0.0014). This lattice strain fluctuation is within the
555 range reported for biogenic (e.g., mollusc shell) and biomimetic calcite [60–63]. HRXRD
556 analysis during *in situ* isochronous heating (annealing) from room T up to 400 °C at
557 50 °C intervals (see Materials and Methods), showed little changes in $\Delta a/a$ and a
558 significant $\Delta c/c$ reduction at T > 200 °C (Figure 5c). Reanalysis of the BCC after
559 annealing at maximum T and subsequent cooling to room T showed permanent
560 lattice contraction and peak broadening (Figure 5). Pokroy et al. [60,61] observed
561 exactly the same features following similar (isochronous annealing) HRXRD analysis
562 of calcite in mollusc shells, demonstrating intracrystalline occlusion of organics (as
563 solutes) in such biominerals. The preferential expansion along the c-axis was

associated with interaction/replacement of carbonate groups placed along (00.1) planes of calcite by acidic proteins, although interaction with other polar planes such as (01.2) should also be favoured [60,63]. The authors also stated that thermal decomposition of occluded organics at T > 200 °C results in strain relaxation and reduction in $\Delta c/c$, with a parallel increase in peak broadening due to reduction in crystallite size and increase in microstrain fluctuations, as we have observed here. Interestingly, we also observed an increase in $\Delta c/c$ of BCC between 100 °C and 200 °C. The latter, also observed in other calcite biominerals such as sea-urchin spicules, has been associated with the presence of ACC and its thermal-induced transformation into calcite, which leads to expansion [64]. Altogether, our HRXRD results confirm that intracrystalline organic occlusions also occur in bacterial calcite, with very similar anisotropic lattice distortion as in other calcite biominerals such as mollusc shells. Our HRXRD results also suggest that intracrystalline ACC is present in the BCC structures, as supported by TEM and ss-NMR results.

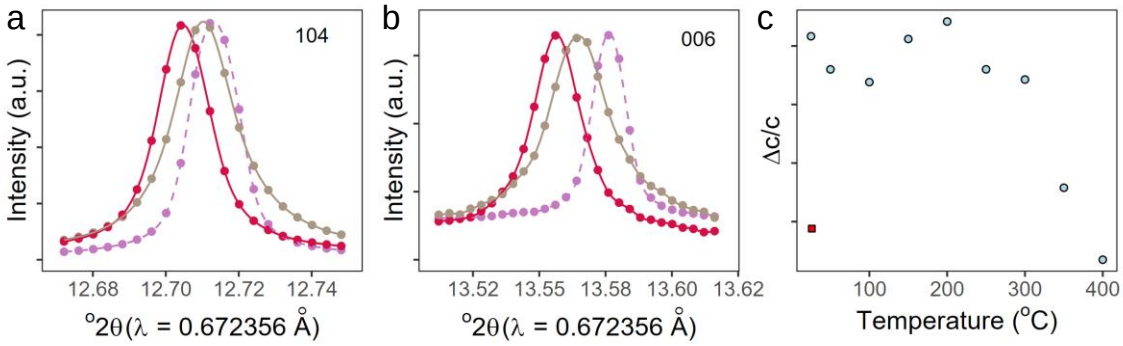

Figure 5. Synchrotron HRXRD analysis of *L. fusiformis* calcite. (a) 104 Bragg peaks and **(b)** 006 Bragg peaks of bacterial calcite before (red) and after annealing at 400 °C and cooling to room T (light brown). The dashed (purple) profiles show the reference Iceland spar calcite; **(c)** T-dependent variation of lattice distortion ($\Delta c/c$) along the c-axis as compared with reference geogenic calcite. The red squared

585 symbol marks the residual lattice distortion after annealing at 400 °C and cooling to
586 room *T*.

587 **Role of crystalline 2D organic films in BCC formation**

588 During TEM imaging of *L. fusiformis* biogenic precipitates we unexpectedly observed
589 layered structures containing areas of amorphous and crystalline carbonates (Figure
590 6a). HRTEM imaging showed that these film-like structures were crystalline
591 displaying lattice fringes oriented in different directions. SAED analysis of the film-
592 like structures revealed diffraction spots with *d*-spacings 3.7 – 4.5 nm aligned in
593 rows with different orientations corresponding to the multiple orientations of the
594 lattice fringes visualized in the HRTEM image (Figure 6a,b yellow and green lines),
595 along with diffraction spots corresponding to (at least two non-oriented) calcite
596 crystals (Figure 6c). The *d*-spacings of the films is at the scale of those measured in
597 protein crystalline structures [65] but full characterization of these structures to confirm
598 if they were made up of proteins was not possible. HRTEM images showed the
599 carbonates closely associated with these 2D crystalline films. The crystalline films
600 were less visible on higher density patches indicating that they were placed at the
601 "bottom" of calcite. However, as shown in Supporting Figure 10a, we could observe
602 in other examples a close relationship between the film and an overlying
603 nanogranular structure, with a SAED pattern corresponding to a calcite single crystal
604 (Supporting Figure 10b). These results suggest that the formation of oriented calcite
605 after particle attachment of ACC is templated by the film underneath, in a similar
606 fashion as that reported on S-layers [66] or carbonic anhydrase films [67] (see
607 Supporting Information).

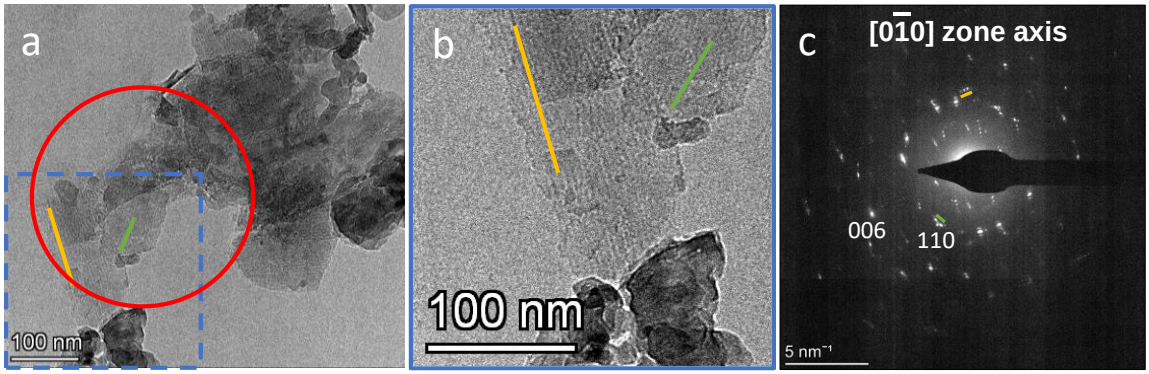

Figure 6. HRTEM analysis of *L. fusiformis* calcite formed on an organic crystalline 2D template. (a) A polycrystal showing different amorphous and crystalline phases, alongside crystalline 2D film showing lattice fringes. **(b)** Zoom-in of the blue squared area in (a) showing lattice fringes in the 2D films. The yellow and green lines show the direction of the lattice fringes. **(c)** SAED pattern of the red circled area in (a) showing different diffraction spots corresponding to calcite ([0$\bar{1}$0] zone axis, calculated using the most intense diffraction spots: note that additional orientations are present) overprinted with diffraction spots of the (organic) films (the green and yellow lines mark the three aligned spots corresponding to the films in (b) with lattice fringes oriented along the green and yellow lines).

Discussion

FESEM showed that the bacteria were closely associated with the BCC crystals and that a nanogranular texture was present, suggesting the formation through an ACC precursor. XRD indicated that all carbonates were calcite, while amorphous and organic signatures were detected with FTIR and TGA in both bleached and unbleached samples. TEM analysis showed the presence of both crystalline and amorphous calcium carbonate, the latter being more predominant in *L. fusiformis*, in

629 agreement with FTIR spectra. In the individual crystals, amorphous areas were
630 present at the rim of the BCCs, likely the growth front of the crystal, in both
631 bacteria. TEM-EDS mapping unveiled the presence of organic-related elements in the
632 bacterial crystals, including N, (and S and P to a lesser extent) associated with both
633 crystalline and amorphous regions of calcium carbonate precipitates. Importantly, we
634 observed low Z-contrast pore areas that resembled a Swiss cheese-like structure
635 thoroughly reported in calcifying metazoans [26,54], and a strong correlation with N was
636 detected in the low Z-contrast regions. CP-MAS C^{13} NMR pointed at the presence of
637 amino acids in a strikingly similar way as in other protein-including calcite
638 biominerals [59]. TEM-EDS and ss-NMR results helped clarify that the observed FTIR
639 bands correspond to amide bonds (Amide I band (1600 – 1700 cm^{-1}); Amide II:
640 1540 cm^{-1} likely attributed to a C=N bond [68] and C-N-C=O bonds at 1499 cm^{-1} [69];
641 Amide III band 1250 – 1350 cm^{-1} [69]). The overall strong indication of amides points
642 to peptides having a role in the biomineralization process, although no particular
643 macromolecule was determined.
644
645 The detection of organic signatures by FTIR and TGA after bleaching suggests that
646 an organic fraction remained bound to the BCCs. Three possibilities exists for this
647 explanation: (i) the bleaching is not sufficient to remove all organics from the
648 precipitate surface, (ii) the organics can also be structurally bound and protected
649 from the bleaching by being occluded in the precipitates, or (iii) both. The presence
650 of organic occlusions in BCCs is as of yet unreported and could have important
651 practical implications while changing our understanding of how biomineralization in
652 bacteria works (see below). While ss-NMR supports the second hypothesis, HRXRD
653 unambiguously shows that this fraction was (in part), intracrystalline organic
654 occlusions. HRXRD shows that the amino acids/peptides are intracrystalline, as there

655 was a marked lattice strain (expansion) along the *c*-axis, and a lattice contraction
656 was observed along the *c*-axis direction after annealing (up to 400 °C). Similar
657 behaviour has been observed using HRXRD in the case of calcite biominerals
658 produced by eukaryotes and their biomimetic counterparts [60–62]. Note that the
659 nanometer-sized porous areas filled with N-rich organics forming the Swiss-cheese
660 structure are, however, too large to account for the lattice strain fluctuations
661 determined by HRXRD. Apparently, organics are occluded in BCCs at two scales: the
662 atomic scale (as solutes in the calcite crystal lattice) resulting in the observed lattice
663 strain, and the mesoscale (as nanometer-sized clusters) as observed here with TEM.
664 This latter nanometer size occlusion could be responsible for the angular spreading
665 observed in SAED patterns and become occluded as the crystal grows at the rim.
666 This is consistent with the amorphous phases occluded inside the crystal lattice
667 observed in HRTEM analysis. Similar organic occlusion occurs in several calcium
668 carbonate biominerals produced by eukaryotes [52]. Note that foreign nanoparticle
669 occlusion results in peak broadening due to microstrain contributions associated with
670 the creation of intracrystalline boundaries acting as a source of inhomogeneous
671 deformation fields but without necessarily contributing to macrostrain, i.e., lattice
672 distortion [61]. These results are consistent with the ss-NMR results as the broad peaks
673 of the CP–MAS ^{13}C NMR spectra point to intracrystalline presence of the amino
674 signatures. Finally, the confirmed role of organics in the crystallization process,
675 explain the preferential growth of BCC calcite along the *c*-axis, with overdeveloped
676 {110} (pseudo)faces, which are typically formed during calcite growth following
677 adsorption of organics on acute steps [70]. Besides the organic signatures, we also
678 report strong indications of ACC presence throughout the whole study, even after
679 bleaching. If the organics remain occluded, then this suggests that ACC is also
680 occluded, and likely stabilized by the organics as observed elsewhere[37]. However,

681 further analysis is needed to unambiguously prove this such as that presented by De
682 Frutos et al. [26].
683
684 The evidence presented here supports the mechanism of precipitation originally
685 alluded to by Enyedi et al. [23], where ACC is stabilized by EPS, and calcite forms
686 through PA. However, we clarify several missing aspects after ACC stabilization.
687 Firstly, we propose that BCC grows by aggregation of protein-stabilized ACC, rather
688 than the more broadly assigned EPS. This is consistent with the intracrystalline
689 occlusion in BCC calcite crystals of both peptides and ACC. Moreover, we observed
690 that larger crystalline 2D films structures, not only stabilize, but act as a template for
691 crystal formation. This film had *d*-spacings in the range of those observed in
692 crystalline protein films, although the molecular features of the films could not be
693 fully characterized. The stabilized ACC then undergoes an amorphous-to-crystalline
694 conversion, at which point the intracrystalline occlusion of a fraction of the organics
695 associated with ACC occurs. This closely resembles the current model of
696 biomineralization of calcite biominerals in eukaryotes [26]. Our proposition is in
697 contrast to what was previously suggested for bacteria, where organics were
698 assumed to be completely ejected [23]. Biomineralization through the eukaryotic model
699 involving an ACC precursor commonly produces a nanogranular structure and results
700 in a Swiss cheese-like structure, as observed here. Even more remarkable, de Frutos
701 and colleagues proposed a model for calcite biomineralization in animals wherein
702 pellicle-like regions of concentrated organics are formed [26]. These are starkly similar
703 to the orderly fashion in which the pore-like N-rich structures were observed in our
704 bacteria biominerals. Moreover, the transformation of ACC nanoparticles into calcite
705 occurs in crystallographic register with the core calcite, which explains the single
706 crystal features of the SAED patterns. Still, some miss-orientation occurs, resulting

707 in the observed angular spreading and the mesocrystal features described above,
708 which are also observed in calcite biominerals produced by eukaryotes, as it is the
709 case of sea-urchin spicules [71]. This could point towards a shared biomineralization
710 process, but future research needs to explore such hypothesis.
711
712 On top of other calcium carbonate biominerals, similar structures as those observed
713 for the BCCs in this work form in biomimetic *in vitro* models [55]. This might not be
714 surprising given that many processes proposed for the formation of calcite
715 biominerals have been shown to be thermodynamically favourable (i.e., down-hill
716 energy landscape) [36]. Yet, critically, in these models the carbonate crystals do not
717 display the highly organized organic-inorganic nanostructure observed in
718 biominerals, in general, and in our BCCs, in particular. Thus, the organization of the
719 BCCs mesocrystals and the hierarchy in organic occlusions observed in this work
720 could contradict the common idea that calcium carbonate biomineral precipitation by
721 microorganisms - in contrast $CaCO_3$ biominerals produced by eukaryotes - is a
722 spontaneous and uncontrolled phenomenon [8]. Furthermore, other authors are
723 already scrutinizing the idea that calcium carbonate biomineralization in prokaryotes
724 is functionless [72]. Some recent work points to real adaptive benefits for MICP. For
725 example, Botusharova et al. [12] showed that bacterial spores could survive
726 entombment in carbonate precipitates, being autoclaved and then reactivated. More
727 recently, it was shown that the precipitation of calcium carbonate had a central role
728 in the effective formation of biofilm in pathogenic bacteria with genetic inhibition of
729 carbonate biomineralization leading to a reduced pathogenicity and biofilm formation
730 [10]. On the other hand, control over the precipitation process could provide protection
731 to the bacteria from unfavourable conditions by controlling the rate and location on
732 the cell where precipitates form, for example to prevent unwanted entombment [66],

733 or reduce damage from toxic metals by removing these from the surrounding
734 environment through (co)precipitation in carbonates [73]. Although the work remains
735 limited, investing energy in producing organics that will create a controlled process
736 of biomineralization might contribute to the inclusive fitness of the organism.
737
738 Aside from the evolutionary standpoint, there is technical applicability to these
739 results. The observations of intracrystalline organics and possibly also ACC, implies
740 that there might be improved mechanical properties for BCCs. Intracrystalline
741 organic matter that occurs in other calcium carbonate biominerals such as mollusk
742 shells, lead to improved mechanical properties (e.g. increased toughness) [52].
743 Moreover, stabilized ACC as a precursor prior to transitioning to calcite has been
744 shown in different biomineral composites to lead to improved structural properties [74].
745 This observations can have implications in the technical applications of microbial
746 biominerals, such as in bioengineering applications of MICP, like self-healing cements
747 or the consolidation of stone built heritage. Moreover, identification of these
748 biosignatures could pave the way for determining biogenicity of carbonate samples in
749 the geologic record, which is not always straight forward. As such, understanding
750 how these mechanisms work and are controlled can open up the door for novel
751 biomaterial applications with purposely designed structure-function.
752
753 **Supporting information**
754 Additional experimental details and results including Supporting Figures 1 – 10 and
755 Supporting Table 1.
756
757 **Acknowledgments**

We thank the personnel of the Centro de Instrumentación Científica (CIC) of the University of Granada for helping with FESEM and TEM analyses and the Inorganic Chemistry department for access to their FTIR. Additional thanks go to the personnel of the Department of Mineralogy and Petrology of the University of Granada for their help with the instrumentations, including Teodora Ilić, Sarah Bonilla Correa, Aurélie Pace and Miguel Burgos Ruiz. Special thanks go to Kerstin Elert for her help with the SEM imaging and Fadwa Jroundi Mesbahi for allowing to grow our bacterial cultures at her facilities. HRXRD experiments were performed at CRYSTAL beamline at SOLEIL Synchrotron with the help of this beamline staff (E. Elkaim). We also thank Julia Atienzar, Aurelie Pace, and Nuria Pujol Solà for their help during HRXRD analyses at SOLEIL synchrotron and Alejandro Rodriguez-Navarro for his help during Rietveld analysis of HRXRD results.

Author Contributions:

FGG contributed Conceptualization, Methodology, Investigation, Visualization, Supervision, Writing (original draft), Writing (review and editing)

MP contributed Conceptualization, Investigation, Visualization, Writing (original draft), Writing (review and editing)

NB contributed Conceptualization, Supervision, Writing (review and editing), Funding acquisition

NDB contributed Conceptualization, Supervision, Writing (review and editing), Funding acquisition

CR-N contributed Conceptualization, Methodology, Investigation, Visualization, Supervision, Writing (original draft), Writing (review and editing), Funding acquisition

Competing Interest Statement: The authors declare no competing interest.

Funding: This work was funded by Spanish Government grant PID2021.125305NB.I00 funded by MCIN/ AEI /10.13039/501100011033 and by ERDF A way of making Europe (to C.R.-N.); Junta de Andalucía and ERDF grant B-RNM-574-UGR20 and research group RNM-179 (to C.R.-N.); University of Granada, Unidad Científica de Excelencia UCE-PP2016-05 (to C.R.-N.). Funding was also provided by the European Union's Horizon 2020 research and innovation programme under Marie Sklodowska-Curie project SUBLime [Grant Agreement n◦955986]. 500 MHz CP-MAS ssNMR was funded by Hercules foundation AUGE/09/2006 and FWO I006920N.

References

(1) Lowestam, H. A.; Weiner, S. *On Biomineralization*, 1st ed.; Oxford University Press: New York, 1989.

(2) Raven, J. A.; Giordano, M. Biomineralization by Photosynthetic Organisms: Evidence of Coevolution of the Organisms and Their Environment? *Geobiology* **2009**, *7* (2), 140–154. https://doi.org/10.1111/j.1472-4669.2008.00181.x.

(3) Addadi, L.; Raz, S.; Weiner, S. Taking Advantage of Disorder: Amorphous Calcium Carbonate and Its Roles in Biomineralization. *Adv. Mater.* **2003**, *15* (12), 959–970. https://doi.org/10.1002/adma.200300381.

(4) Schopf, J. W. Solution to Darwin's Dilemma: Discovery of the Missing Precambrian Record of Life. *Proc. Natl. Acad. Sci. U. S. A.* **2000**, *97* (13), 6947–6953. https://doi.org/10.1073/pnas.97.13.6947.

(5) Boquet, E.; Boronat, A.; Ramos-Cormenzana, A. Production of Calcite (Calcium Carbonate) Crystals by Soil Bacteria Is a General Phenomenon. *Am. J. Med.*

Sci. **1973**, *242* (2), 527. https://doi.org/10.1097/00000441-196108000-00035.

(6) Fujita, Y.; Grant Ferris, F.; Daniel Lawson, R.; Colwell, F. S.; Smith, R. W. Calcium Carbonate Precipitation by Ureolytic Subsurface Bacteria. *Geomicrobiol. J.* **2000**, *17* (4), 305–318. https://doi.org/10.1080/782198884.

(7) Seifan, M.; Berenjian, A. Microbially Induced Calcium Carbonate Precipitation: A Widespread Phenomenon in the Biological World. *Appl. Microbiol. Biotechnol.* **2019**, *103* (12), 4693–4708. https://doi.org/10.1007/s00253-019-09861-5.

(8) Frankel, R. B.; Bazylinski, D. Biologically Induced Mineralization by Bacteria. *Rev. Mineral. Geochemistry* **2003**, *54* (1), 95–114. https://doi.org/10.2113/0540095.

(9) Cosmidis, J.; Benzerara, K. Why Do Microbes Make Minerals? *Comptes Rendus - Geosci.* **2022**, *354* (1), 1–39. https://doi.org/10.5802/CRGEOS.107.

(10) Cohen-Cymberknoh, M.; Kolodkin-Gal, D.; Keren-Paz, A.; Peretz, S.; Brumfeld, V.; Kapishnikov, S.; Suissa, R.; Shteinberg, M.; McLeod, D.; Maan, H.; Patrauchan, M.; Zamir, G.; Kerem, E.; Kolodkin-Gal, I. Calcium Carbonate Mineralization Is Essential for Biofilm Formation and Lung Colonization. *iScience* **2022**, *25* (5), 104234. https://doi.org/10.1016/j.isci.2022.104234.

(11) Oppenheimer-Shaanan, Y.; Sibony-Nevo, O.; Bloom-Ackermann, Z.; Suissa, R.; Steinberg, N.; Kartvelishvily, E.; Brumfeld, V.; Kolodkin-Gal, I. Spatio-Temporal Assembly of Functional Mineral Scaffolds within Microbial Biofilms. *npj Biofilms Microbiomes* **2016**, *2*, 15031. https://doi.org/10.1038/npjbio.

(12) Botusharova, S.; Gardner, D.; Harbottle, M. Augmenting Microbially Induced Carbonate Precipitation of Soil with the Capability to Self-Heal. *J. Geotech. Geoenvironmental Eng.* **2020**, *146* (4), 04020010. https://doi.org/10.1061/(asce)gt.1943-5606.0002214.

(13) Baumgartner, L. K.; Reid, R. P.; Dupraz, C.; Decho, A. W.; Buckley, D. H.; Spear, J. R.; Przekop, K. M.; Visscher, P. T. Sulfate Reducing Bacteria in Microbial Mats: Changing Paradigms, New Discoveries. *Sediment. Geol.* **2006**, *185* (3-4 SPEC. ISS.), 131–145. https://doi.org/10.1016/j.sedgeo.2005.12.008.

(14) Erşan, Y. Ç.; De Belie, N.; Boon, N. Microbially Induced CaCO3 Precipitation through Denitrification: An Optimization Study in Minimal Nutrient Environment. *Biochem. Eng. J.* **2015**, *101*, 108–118. https://doi.org/10.1016/j.bej.2015.05.006.

(15) Stocks-Fischer, S.; Galinat, J. K.; Bang, S. S. Microbiological Precipitation of CaCO3. *Soil Biol. Biochem.* **1999**, *31* (11), 1563–1571. https://doi.org/10.1016/S0038-0717(99)00082-6.

(16) Rivadeneyra, M. A.; Delgado, R.; Moral, A.; Ferrer, M. R.; Ramos-Cormenzana, A. Precipatation of Calcium Carbonate by Vibrio Spp. from an Inland Saltern. *FEMS Microbiol. Ecol.* **1994**, *13* (3), 197–204. https://doi.org/10.1111/j.1574-6941.1994.tb00066.x.

(17) Ehrlich, H. L. *Ehrlich's Geomicrobiology*, Sixth.; Ehrlich, H. L., Newman, D. K., Kappler, A., Eds.; Taylor & Francis, 2016.

(18) Tourney, J.; Ngwenya, B. T. The Role of Bacterial Extracellular Polymeric Substances in Geomicrobiology. *Chem. Geol.* **2014**, *386*, 115–132. https://doi.org/10.1016/j.chemgeo.2014.08.011.

(19) Benzerara, K.; Menguy, N.; López-García, P.; Yoon, T. H.; Kazmierczak, J.; Tyliszczak, T.; Guyot, F.; Brown, G. E. Nanoscale Detection of Organic Signatures in Carbonate Microbialites. *Proc. Natl. Acad. Sci. U. S. A.* **2006**, *103* (25), 9440–9445. https://doi.org/10.1073/pnas.0603255103.

(20) Lyu, J.; Li, F.; Long, H.; Zhu, X.; Fu, N.; Guo, Z.; Zhang, W. Bacterial

Templated Carbonate Mineralization: Insights from Concave-Type Crystals Induced by Curvibacter Lanceolatus Strain HJ-1. *RSC Advances*. 2024, pp 353–363. https://doi.org/10.1039/d3ra06803j.

(21) Lyu, J.; Qin, W.; Zhang, C.; Li, F. Nanoparticle Accumulation in Microbial Induced Carbonate Precipitation: The Crucial Role of Extracellular Polymeric Substance. *Geomicrobiol. J.* **2020**, *0* (0), 837–847. https://doi.org/10.1080/01490451.2020.1786866.

(22) Chen, L.; Shen, Y.; Xie, A.; Huang, B.; Jia, R.; Guo, R.; Tang, W. Bacteria-Mediated Synthesis of Metal Carbonate Minerals with Unusual Morphologies and Structures. *Cryst. Growth Des.* **2009**, *9* (2), 743–754. https://doi.org/10.1021/cg800224s.

(23) Enyedi, N. T.; Makk, J.; Kótai, L.; Berényi, B.; Klébert, S.; Sebestyén, Z.; Molnár, Z.; Borsodi, A. K.; Leél-Őssy, S.; Demény, A.; Németh, P. Cave Bacteria-Induced Amorphous Calcium Carbonate Formation. *Sci. Rep.* **2020**, *10* (1), 1–12. https://doi.org/10.1038/s41598-020-65667-w.

(24) Marvasi, M.; Gallagher, K. L.; Martinez, L. C.; Molina Pagan, W. C.; Rodríguez Santiago, R. E.; Castilloveitía Vega, G.; Visscher, P. T. Importance of B4 Medium in Determining Organomineralization Potential of Bacterial Environmental Isolates. *Geomicrobiol. J.* **2012**, *29* (10), 916–924. https://doi.org/10.1080/01490451.2011.636145.

(25) Seifan, M.; Samani, A. K.; Berenjian, A. Induced Calcium Carbonate Precipitation Using Bacillus Species. *Appl. Microbiol. Biotechnol.* **2016**, *100* (23), 9895–9906. https://doi.org/10.1007/s00253-016-7701-7.

(26) de Frutos, M.; Rodríguez-Navarro, A. B.; Li, X.; Checa, A. G. Nanoscale Analysis of the Structure and Composition of Biogenic Calcite Reveals the Biomineral Growth Pattern. *ACS Nano* **2023**, *17* (3), 2829–2839.

https://doi.org/10.1021/acsnano.2c11169.

(27) Rietveld, H. M. Line Profiles of Neutron Powder-Diffraction Peaks for Structure Refinement. *Acta Crystallogr.* **1967**, *22* (1), 151–152. https://doi.org/10.1107/s0365110x67000234.

(28) Markgraf, S. A.; Reeder, R. J. High-Temperature Structure Refinements of Calcite and Magnesite. *Am. Mineral.* **1985**, *70* (5), 590–600.

(29) Yan, H.; Han, Z.; Zhao, H.; Pan, J.; Zhao, Y.; Tucker, M. E.; Zhou, J.; Yan, X.; Yang, H.; Fan, D. The Bio-Precipitation of Calcium and Magnesium Ions by Free and Immobilized Lysinibacillus Fusiformis DB1-3 in the Wastewater. *J. Clean. Prod.* **2020**, *252*, 119826. https://doi.org/10.1016/j.jclepro.2019.119826.

(30) Park, S. J.; Park, Y. M.; Chun, W. Y.; Kim, W. J.; Ghim, S. Y. Calcite-Forming Bacteria for Compressive Strength Improvement in Mortar. *J. Microbiol. Biotechnol.* **2010**, *20* (4), 782–788. https://doi.org/10.4014/JMB.0911.11015.

(31) Chekroun, K. Ben; Rodríguez-Navarro, C.; González-Muñoz, M. T.; Arias, J. M.; Cultrone, G.; Rodríguez-Gallego, M. Precipitation and Growth Morphology of Calcium Carbonate Induced by Myxococcus Xanthus: Implications for Recognition of Bacterial Carbonates. *J. Sediment. Res.* **2004**, *74* (6), 868–876. https://doi.org/10.1306/050504740868.

(32) Gilbert, P. U. P. A.; Bergmann, K. D.; Boekelheide, N.; Tambutté, S.; Mass, T.; Marin, F.; Adkins, J. F.; Erez, J.; Gilbert, B.; Knutson, V.; Cantine, M.; Hernández, J. O.; Knoll, A. H. Biomineralization: Integrating Mechanism and Evolutionary History. *Sci. Adv.* **2022**, *8* (10). https://doi.org/10.1126/sciadv.abl9653.

(33) Rodriguez-Navarro, C.; Burgos Cara, A.; Elert, K.; Putnis, C. V.; Ruiz-Agudo, E. Direct Nanoscale Imaging Reveals the Growth of Calcite Crystals via

Amorphous Nanoparticles. *Cryst. Growth Des.* **2016**, *16* (4), 1850–1860. https://doi.org/10.1021/acs.cgd.5b01180.

(34) De Yoreo, J. J.; Gilbert, P. U. P. A.; Sommerdijk, N. A. J. M.; Penn, R. L.; Whitelam, S.; Joester, D.; Zhang, H.; Rimer, J. D.; Navrotsky, A.; Banfield, J. F.; Wallace, A. F.; Michel, F. M.; Meldrum, F. C.; Cölfen, H.; Dove, P. M. Crystallization by Particle Attachment in Synthetic, Biogenic, and Geologic Environments. *Science (80-.).* **2015**, *349* (6247). https://doi.org/10.1126/science.aaa6760.

(35) Wolf, S. E.; Böhm, C. F.; Harris, J.; Demmert, B.; Jacob, D. E.; Mondeshki, M.; Ruiz-Agudo, E.; Rodríguez-Navarro, C. Nonclassical Crystallization in Vivo et in Vitro (I): Process-Structure-Property Relationships of Nanogranular Biominerals. *J. Struct. Biol.* **2016**, *196* (2), 244–259. https://doi.org/10.1016/j.jsb.2016.07.016.

(36) Rodríguez-Navarro, C.; Ruiz-Agudo, E.; Harris, J.; Wolf, S. E. Nonclassical Crystallization in Vivo et in Vitro (II): Nanogranular Features in Biomimetic Minerals Disclose a General Colloid-Mediated Crystal Growth Mechanism. *J. Struct. Biol.* **2016**, *196* (2), 260–287. https://doi.org/10.1016/j.jsb.2016.09.005.

(37) Gong, Y. U. T.; Killian, C. E.; Olson, I. C.; Appathurai, N. P.; Amasino, A. L.; Martin, M. C.; Holt, L. J.; Wilt, F. H.; Gilbert, P. U. P. A. Phase Transitions in Biogenic Amorphous Calcium Carbonate. *Proc. Natl. Acad. Sci. U. S. A.* **2012**, *109* (16), 6088–6093. https://doi.org/10.1073/PNAS.1118085109/SUPPL_FILE/SM02.MOV.

(38) DeOliveira, D. B.; Laursen, R. A. Control of Calcite Crystal Morphology by a Peptide Designed to Bind to a Specific Surface. *J. Am. Chem. Soc.* **1997**, *119* (44), 10627–10631. https://doi.org/10.1021/ja972270w.

(39) Teng, H. H.; Dove, P. M. Surface Site-Specific Interactions of Aspartate with Calcite during Dissolution: Implications for Biomineralization. *Am. Mineral.* **1997**, *82* (9–10), 878–887. https://doi.org/10.2138/am-1997-9-1005.

(40) Rodríguez-Navarro, A. B.; Marie, P.; Nys, Y.; Hincke, M. T.; Gautron, J. Amorphous Calcium Carbonate Controls Avian Eggshell Mineralization: A New Paradigm for Understanding Rapid Eggshell Calcification. *J. Struct. Biol.* **2015**, *190* (3), 291–303. https://doi.org/10.1016/j.jsb.2015.04.014.

(41) Beniash, E.; Aizenberg, J.; Addadi, L.; Weiner, S. Amorphous Calcium Carbonate Transforms into Calcite during Sea Urchin Larval Spicule Growth. *Proc. R. Soc. B Biol. Sci.* **1997**, *264* (1380), 461–465. https://doi.org/10.1098/rspb.1997.0066.

(42) Ihli, J.; Wong, W. C.; Noel, E. H.; Kim, Y. Y.; Kulak, A. N.; Christenson, H. K.; Duer, M. J.; Meldrum, F. C. Dehydration and Crystallization of Amorphous Calcium Carbonate in Solution and in Air. *Nat. Commun.* **2014**, *5*, 1–10. https://doi.org/10.1038/ncomms4169.

(43) Mehta, N.; Gaëtan, J.; Giura, P.; Azaïs, T.; Benzerara, K. Detection of Biogenic Amorphous Calcium Carbonate (ACC) Formed by Bacteria Using FTIR Spectroscopy. *Spectrochim. Acta - Part A Mol. Biomol. Spectrosc.* **2022**, *278*, 121262. https://doi.org/10.1016/j.saa.2022.121262.

(44) Ryparová, P.; Prošek, Z.; Schreiberová, H.; Bílý, P.; Tesárek, P. The Role of Bacterially Induced Calcite Precipitation in Self-Healing of Cement Paste. *J. Build. Eng.* **2021**, *39* (October 2020). https://doi.org/10.1016/j.jobe.2021.102299.

(45) Pavia, D. L.; Lampman, G. M.; Kriz, G. S.; Vyvyan, J. R. Infrared Spectroscopy. In *Introduction to Spectroscopy*; Cengage Learning: Stamford, CT, 2015; pp 14–106. https://doi.org/10.1016/S1460-1567(00)80010-0.

(46) Schmidt, M. P.; Ilott, A. J.; Phillips, B. L.; Reeder, R. J. Structural Changes upon Dehydration of Amorphous Calcium Carbonate. *Cryst. Growth Des.* **2014**, *14* (3), 938–951. https://doi.org/10.1021/cg401073n.

(47) Rodríguez-Navarro, A. B.; Grenier, C.; Checa, A. G.; Jiménez-López, C.; Sánchez-Sánchez, P.; Bertone, D.; Lagos, N. A. Role of the Organic Matter in the Structural Organization of Giant Barnacle Austromegabalanus Psittacus Shell from the Micro- To Nanoscale. *Cryst. Growth Des.* **2021**, *21* (1), 357–365. https://doi.org/10.1021/acs.cgd.0c01222.

(48) Valverde, J. M.; Perejon, A.; Medina, S.; Perez-Maqueda, L. A. Thermal Decomposition of Dolomite under CO2: Insights from TGA and in Situ XRD Analysis. *Phys. Chem. Chem. Phys.* **2015**, *17* (44), 30162–30176. https://doi.org/10.1039/c5cp05596b.

(49) Cölfen, H.; Antonietti, M. Mesocrystals: Inorganic Superstructures Made by Highly Parallel Crystallization and Controlled Alignment. *Angew. Chemie - Int. Ed.* **2005**, *44* (35), 5576–5591. https://doi.org/10.1002/anie.200500496.

(50) Bergström, L.; Sturm née Rosseeva, E. V.; Salazar-Alvarez, G.; Cölfen, H. Mesocrystals in Biominerals and Colloidal Arrays. *Acc. Chem. Res.* **2015**, *48* (5), 1391–1402. https://doi.org/10.1021/ar500440b.

(51) Towe, K. M.; Thompson, G. R. The Structure of Some Bivalve Shell Carbonates Prepared by Ion-Beam Thinning - A Comparison Study. *Calcif. Tissue Res.* **1972**, *10* (1), 38–48. https://doi.org/10.1007/BF02012534.

(52) Deng, Z.; Jia, Z.; Li, L. Biomineralized Materials as Model Systems for Structural Composites: Intracrystalline Structural Features and Their Strengthening and Toughening Mechanisms. *Adv. Sci.* **2022**, *9*, 2103524. https://doi.org/10.1002/advs.202103524.

(53) Rodriguez-Navarro, C.; Ruiz-Agudo, E.; Luque, A.; Rodriguez-Navarro, A. B.;

Ortega-Huertas, M. Thermal Decomposition of Calcite: Mechanisms of Formation and Textural Evolution of CaO Nanocrystals. *Am. Mineral.* **2009**, *94* (4), 578–593. https://doi.org/10.2138/am.2009.3021.

(54) Li, H.; Xin, H. L.; Kunitake, M. E.; Keene, E. C.; Muller, D. A.; Estroff, L. A. Calcite Prisms from Mollusk Shells (Atrina Rigida): Swiss-Cheese-like Organic-Inorganic Single-Crystal Composites. *Adv. Funct. Mater.* **2011**, *21* (11), 2028–2034. https://doi.org/10.1002/adfm.201002709.

(55) Li, H.; Xin, H. L.; Muller, D. A.; Estroff, L. A. Visualizing the 3D Internal Structure of Agarose Hydrogels. *Science (80-.).* **2009**, *326* (November), 1244–1247.

(56) Nebel, H.; Neumann, M.; Mayer, C.; Epple, M. On the Structure of Amorphous Calcium Carbonate - A Detailed Study by Solid-State NMR Spectroscopy. *Inorg. Chem.* **2008**, *47* (17), 7874–7879. https://doi.org/10.1021/ic8007409.

(57) Chaloupecká, E.; Tyrpekl, V.; Bártová, K.; Nishiyama, Y.; Dračínský, M. NMR Crystallography of Amino Acids. *Solid State Nucl. Magn. Reson.* **2024**, *130* (November 2023). https://doi.org/10.1016/j.ssnmr.2024.101921.

(58) Pisklak, D. M. I.; Szeleszczuk, Ł.; Wawer, I. 1H and 13C Magic-Angle Spinning Nuclear Magnetic Resonance Studies of the Chicken Eggshell. *J. Agric. Food Chem.* **2012**, *60* (50), 12254–12259. https://doi.org/10.1021/jf304230g.

(59) Kababya, S.; Ben Shir, I.; Schmidt, A. From Molecular Level to Macroscopic Properties: A Solid-State NMR Biomineralization and Biomimetic Exploration. *Curr. Opin. Colloid Interface Sci.* **2022**, *62*, 101630. https://doi.org/10.1016/j.cocis.2022.101630.

(60) Pokroy, B.; Fitch, A. N.; Marin, F.; Kapon, M.; Adir, N.; Zolotoyabko, E. Anisotropic Lattice Distortions in Biogenic Calcite Induced by Intra-Crystalline Organic Molecules. *J. Struct. Biol.* **2006**, *155* (1), 96–103.

https://doi.org/10.1016/j.jsb.2006.03.008.

(61) Pokroy, B.; Fitch, A. N.; Zolotoyabko, E. The Microstructure of Biogenic Calcite: A View by High-Resolution Synchrotron Powder Diffraction. *Adv. Mater.* **2006**, *18* (18), 2363–2368. https://doi.org/10.1002/adma.200600714.

(62) Aizenberg, J.; Hanson, J.; Koetzle, T. F.; Weiner, S.; Addadi, L. Control of Macromolecule Distribution within Synthetic and Biogenic Single Calcite Crystals. *J. Am. Chem. Soc.* **1997**, *119* (5), 881–886. https://doi.org/10.1021/ja9628821.

(63) Lang, A.; Mijowska, S.; Polishchuk, I.; Fermani, S.; Falini, G.; Katsman, A.; Marin, F.; Pokroy, B. Acidic Monosaccharides Become Incorporated into Calcite Single Crystals**. *Chem. - A Eur. J.* **2020**, *26* (70), 16860–16868. https://doi.org/10.1002/chem.202003344.

(64) Albéric, M.; Caspi, E. N.; Bennet, M.; Ajili, W.; Nassif, N.; Azaïs, T.; Berner, A.; Fratzl, P.; Zolotoyabko, E.; Bertinetti, L.; Politi, Y. Interplay between Calcite, Amorphous Calcium Carbonate, and Intracrystalline Organics in Sea Urchin Skeletal Elements. *Cryst. Growth Des.* **2018**, *18* (4), 2189–2201. https://doi.org/10.1021/acs.cgd.7b01622.

(65) Stevenson, H. P.; Makhov, A. M.; Calero, M.; Edwards, A. L.; Zeldin, O. B.; Mathews, I. I.; Lin, G.; Barnes, C. O.; Santamaria, H.; Ross, T. M.; Soltis, S. M.; Khosla, C.; Nagarajan, V.; Conway, J. F.; Cohen, A. E.; Calero, G. Use of Transmission Electron Microscopy to Identify Nanocrystals of Challenging Protein Targets. *Proc. Natl. Acad. Sci. U. S. A.* **2014**, *111* (23), 8470–8475. https://doi.org/10.1073/pnas.1400240111.

(66) Schultze-Lam, S.; Beveridge, T. J. Nucleation of Celestite and Strontianite on a Cyanobacterial S-Layer. *Appl. Environ. Microbiol.* **1994**, *60* (2).

(67) Rodriguez-Navarro, C.; Cizer, Ö.; Kudłacz, K.; Ibañez-Velasco, A.; Ruiz-

Agudo, C.; Elert, K.; Burgos-Cara, A.; Ruiz-Agudo, E. The Multiple Roles of Carbonic Anhydrase in Calcium Carbonate Mineralization. *CrystEngComm* **2019**, *21* (48), 7407–7423. https://doi.org/10.1039/c9ce01544b.

(68) Murdock, J. N.; Wetzel, D. L. FT-IR Microspectroscopy Enhances Biological and Ecological Analysis of Algae. *Appl. Spectrosc. Rev.* **2009**, *44* (4), 335–361. https://doi.org/10.1080/05704920902907440.

(69) Ji, Y.; Yang, X.; Ji, Z.; Zhu, L.; Ma, N.; Chen, D.; Jia, X.; Tang, J.; Cao, Y. DFT-Calculated IR Spectrum Amide I, II, and III Band Contributions of N-Methylacetamide Fine Components. *ACS Omega*. 2020, pp 8572–8578. https://doi.org/10.1021/acsomega.9b04421.

(70) Kim, Y. Y.; Ganesan, K.; Yang, P.; Kulak, A. N.; Borukhin, S.; Pechook, S.; Ribeiro, L.; Kröger, R.; Eichhorn, S. J.; Armes, S. P.; Pokroy, B.; Meldrum, F. C. An Artificial Biomineral Formed by Incorporation of Copolymer Micelles in Calcite Crystals. *Nat. Mater.* **2011**, *10* (11), 890–896. https://doi.org/10.1038/nmat3103.

(71) Seto, J.; Ma, Y.; Davis, S. A.; Meldrum, F.; Gourrier, A.; Kim, Y. Y.; Schilde, U.; Sztucki, M.; Burghammer, M.; Maltsev, S.; Jäger, C.; Cölfen, H. Structure-Property Relationships of a Biological Mesocrystal in the Adult Sea Urchin Spine. *Proc. Natl. Acad. Sci. U. S. A.* **2012**, *109* (10), 3699–3704. https://doi.org/10.1073/pnas.1109243109.

(72) Cosmidis, J.; Benzerara, K. Comptes Rendus Géoscience Why Do Microbes Make Minerals ? *Comptes Rendus - Géoscience Sci. la Planète* **2022**, *354*, 0–39. https://doi.org/10.5802/crgeos.107.

(73) Mugwar, A. J.; Harbottle, M. J. Toxicity Effects on Metal Sequestration by Microbially-Induced Carbonate Precipitation. *J. Hazard. Mater.* **2016**, *314*, 237–248. https://doi.org/10.1016/j.jhazmat.2016.04.039.

(74) Albéric, M.; Bertinetti, L.; Zou, Z.; Fratzl, P.; Habraken, W.; Politi, Y. The Crystallization of Amorphous Calcium Carbonate Is Kinetically Governed by Ion Impurities and Water. *Adv. Sci.* **2018**, *5* (5). https://doi.org/10.1002/advs.201701000.